ACS APPLIED MATERIALS & INTERFACES

www.acsami.org

Research Article

Solution-Processed $Pb(Zr,Ti)O_3$ Thin Films with Strong Remnant Pockels Coefficient

Ewout Picavet, Kobe De Geest, Enes Lievens, Hannes Rijckaert, Tom Vandekerckhove, Eduardo Solano, Davy Deduytsche, Laura Van Bossele, Dries Van Thourhout, Klaartje De Buysser,* and Jeroen Beeckman*

Cite This: *ACS Appl. Mater. Interfaces* 2024, 16, 41134–41144

Read Online

ACCESS | Metrics & More | Article Recommendations | Supporting Information

ABSTRACT: In contrast to the widely studied electrical properties of $Pb(Zr,Ti)O_3$ thin films, which have led to their applicability in various application areas such as thin film capacitors, microelectronics, and ferroelectric memories, the electro-optic (EO) properties are far less studied, which hinders the applicability of $Pb(Zr,Ti)O_3$ films for EO applications such as heterogeneously integrated phase modulators in silicon (Si) photonics. Therefore, the EO properties of $Pb(Zr,Ti)O_3$ films need to be further investigated to pave the way for the applicability of $Pb(Zr,Ti)O_3$ films in EO applications. As the EO properties of ferroelectric thin films strongly depend on their crystal phase and texture, which in turn are influenced by the method of film fabrication. Therefore, in this work, we investigate the EO properties of a promising solution process using a $La_2O_2CO_3$ template film. We successively characterize the precursor ink, microstructure and EO properties of the solution-processed $Pb(Zr,Ti)O_3$film. The $Pb(Zr,Ti)O_3$ film exhibits a fiber texture and has a large maximum and remnant Pockels coefficient (r_{eff}) of 69 pm V^{-1} and 66 pm V^{-1}, respectively. The integration into a ring resonator-based modulator shows a $V_\pi L$ of 2.019 V cm. The determination of these promising EO properties could further pave the way for the applicability of $Pb(Zr,Ti)O_3$ thin films in Si photonics.

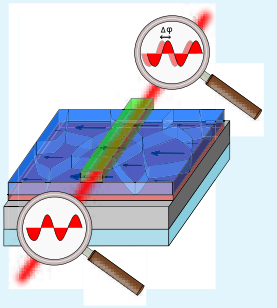

KEYWORDS: *$La_2O_2CO_3$ template film, $Pb(Zr,Ti)O_3$ film, Fiber texture, Nanophotonic Pockels modulator, SiN*

INTRODUCTION

The numerous excellent material properties of $Pb(Zr,Ti)O_3$ have driven research for several decades as they exhibit high piezoelectric coefficients useful for a variety of microelectronic applications,[1−3] their high dielectric constant is attractive for thin film capacitors,[4,5] and their high residual polarization is essential for nonvolatile ferroelectric memories.[6] In addition to these electrical properties, the strong electro-optic (EO) effect (Pockels effect) has also attracted much attention in recent years to obtain heterogeneously integrated phase modulators in silicon (Si) photonics. A simplified description of the Pockels effect is given by a linear relationship between the change in refractive index ($\Delta n(E)$) due to an applied external electric field (E) according to the following equation:

$$\Delta n(E) = -\frac{1}{2} r_{eff} n_0^3 E \quad (1)$$

In this equation, r_{eff} (pm V^{-1}) is the effective Pockels coefficient, n_0 is the refractive index in the absence of an electric field and E (V cm^{-1}) is the applied electric field. Among the alternative ferroelectric materials currently being investigated for the fabrication of heterogeneous phase modulators, the material $Pb(Zr,Ti)O_3$ is one of the most promising candidates for two main reasons. First, $Pb(Zr,Ti)O_3$ can be poled and exhibits a strong and stable remnant polarization, which is in contrast to other materials such as $KNbO_3$, $BaTiO_3$, $(Sr,Ba)Nb_2O_3$, which have a lower remnant polarization.[7−10] Second, the $Pb(Zr,Ti)O_3$ material has one of the highest Curie temperatures (T_c) (450 °C) of all ferroelectric materials, which ensures very high thermal stability and a high working temperature.[11,12]

Although the $Pb(Zr,Ti)_3$ films have already found their way into various applications due to their electrical properties, their EO properties are far less explored, which drastically limits the applicability of the ferroelectric film in Si photonics and the subsequent development of photonic devices. Consequently, there is a need to investigate the EO properties of $Pb(Zr,Ti)O_3$ films to pave the way for the integration of $Pb(Zr,Ti)O_3$ films into Si photonics. However, the EO properties are highly dependent on the crystal phase and the texture of the films, which in turn are influenced by the film fabrication method. Over the years, high quality $Pb(Zr,Ti)O_3$ films have been fabricated via methods such as chemical solution deposition (CSD),[13,14] RF sputtering,[15−17] and pulsed laser deposition

Received: April 30, 2024
Revised: July 9, 2024
Accepted: July 15, 2024
Published: July 30, 2024

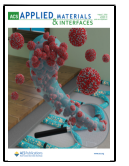

(PLD).[18,19] In this work, the fabrication method is based on previous work in which a $La_2O_2CO_3$ template film was used in combination with the chemical solution deposition (CSD) process.[20,21] This promising route ensures compatibility with different photonic platforms via the $La_2O_2CO_3$ template film, while the CSD process enables easy tunability of the Zr/Ti ratio. A $Pb(Zr,Ti)O_3$ ink with a Zr/Ti = 52/48 is targeted as this ensures superior EO properties,[22] which is related to the possible coexistence of the two ferroelectric $Pb(Zr,Ti)O_3$ phases: tetragonal and rhombohedral.[23,24] Subsequently, since the EO properties of the $Pb(Zr,Ti)O_3$ films strongly depend on their crystal phase and film texture, we will first determine the microstructural properties of the $Pb(Zr,Ti)O_3$ film. Finally, the EO properties are determined via an free-space transmission setup as well as via an integrated $Pb(Zr,Ti)O_3$ SiN O-band ring resonator.

In order to achieve a stable $Pb(Zr,Ti)O_3$ ink, acetylacetonate was added as a complexing agent to stabilize the Ti and Zr precursors. Subsequent annealing yielded a predominantly rhombohedral $Pb(Zr,Ti)O_3$ phase ($R3m$) and a fiber texture, as well as a characteristic microstructure and low surface roughness. This highly textured film yields a large maximum r_{eff} and an almost similar remnant r_{eff} which is very stable over time. In summary, the EO characterization of the fabricated $Pb(Zr,Ti)O_3$ film is a next step toward the integration of $Pb(Zr,Ti)O_3$ films in Si photonics.

EXPERIMENTAL SECTION

$Pb(Zr,Ti)O_3$ Ink Formulation, Deposition, and Characterization. Prior to deposition, the substrates were ultrasonically cleaned with acetone, isopropanol, and distilled water for 5 min and then heated on a hot plate at 120 °C in an ambient atmosphere to remove solvent residues. A two-step manufacturing process is introduced for the production of the crystalline $Pb(Zr,Ti)O_3$ film. First, a $La_2O_2CO_3$ template film was deposited as previously reported.[20] Subsequently, the $Pb(Zr,Ti)O_3$ precursor solution (Zr/Ti: 52/48) was prepared based on a modified sol–gel method by dissolving lead acetate (Merck, ≥99%), zirconium butoxide (Merck, 80 wt % in 1-butanol), and titanium butoxide (Merck, 97%) plus additives in 1-butanol (Merck, ≥99%). Hacac (Merck, ≥99%) was used as a complexing agent in a ratio of 1:1 with the Ti and Zr precursor. A final molarity of 0.4 M was achieved and the ink was filtered with a 0.2 μm PET filter before deposition. The precursor solution was spin-coated at a spin speed of 3000 rpm for 30 s using a KLM SCC-200 model. Finally, the wet film was pyrolyzed at 200 °C for 10 min in ambient atmosphere and then annealed in a Jipelec jetfirst 150 rapid thermal annealing (RTA) furnace under O_2 flow of 600 scc min^{-1} at an annealing temperature of 600 °C for 30 min to obtain highly crystalline $Pb(Zr,Ti)_3$ films.[14] Metal complexation in the precursor solution was characterized by means of attenuated total reflection-Fourier transform infrared spectroscopy (ATR-FTIR) performed on a PerkinElmer FTIR spectrum 1000, equipped with a HATR module.

Phase Composition, Texture, and Surface Characterization. Phase composition and texture of the $Pb(Zr,Ti)O_3$ thin film were characterized by grazing incident wide-angle X-ray scattering (GIWAXS), θ-2θ XRD measurements, pole figures and high-resolution (HR) transmission electron microscopy (TEM). The GIWAXS data was obtained at NCD-SWEET beamline at the ALBA Synchrotron Radiation Facility (Spain). The incident X-ray beam energy was set to 12.4 keV (λ = 0.9998 Å) using a channel cut Si (111) monochromator. An array of Be lenses was used to collimate the beam, resulting in a beam size of 50 × 150 μm^2 (V × H) at the sample position. The angle of incidence α_i was screened between 0° and 1° and finally set at 0.325° ensuring surface sensitivity. An exposure time of 10 s was used. The scattering patterns were recorded using a Rayonix LX255-HS area detector, which consists of an array of 1920 × 5760 pixels (H × V) with a pixel size of 44.27 × 44.27 μm^2. The scattering vector—q—was calibrated using Cr_2O_3 as a standard sample, obtaining a sample-to-detector distance of 201.65 mm. The intrinsic 2D GIWAXS pattern is corrected as a function of the components of the scattering vector and was reported here after integration and conversion of the scattering vector (q) to 2θ. The θ-2θ XRD measurements were performed on a Bruker D8 Advance diffractometer (Cu–Kα λ = 1.54184 Å) equipped with a LynxEye XE-T Silicon strip line detector. The diffraction was measured between 2θ = 20° and 50° with a step width of 0.02°, step time of 4 s and an additional Ni filter. Subsequently, a Lotgeringsfactor (LF) is calculated from the XRD intensities (20°–70°), and is defined as the following equation: $LF = (p - p_0)/(1 - p_0)$, where p denotes the fraction of the summation of the peak intensities corresponding to the preferred orientation axis to that of the summation of all diffraction peaks in particle-oriented materials. p_0 is p of the material with a random particle distribution. The LF varies between 0 and 1, LF = 0 corresponds to random orientation, and LF = 1 to perfect orientation.[25] Pole figure measurements of the film were determined using a Panalytical Empyrean XRD with Cu K_α radiation, Bragg–Brentano HD beam conditioning, five-axis goniometer, and PixCel3D detector. HRTEM images were acquired on a JEOL JEM-2200FS TEM at Ghent University TEM core facility operated at 200 kV and equipped with Cs corrector. For the TEM measurements, a cross-sectional TEM lamella was prepared using in situ lift out procedure on the FEI Nova 600 Nanolab Dual Beam focused ion beam (FIB) SEM. The surface microstructure of the $Pb(Zr,Ti)O_3$ films was analyzed by scanning electron microscopy (SEM) using a JEOL FEG SEM JSM-7600F at an accelerating voltage of 10 kV. The surface roughness of the film was determined by atomic force microscopy (AFM) using a Bruker Dimension Edge system in tapping mode in air. The root-mean-square (RMS) of the roughness values was calculated using 3 × 3 μm^2 micrographs.

Electro-optic Characterization. In order to quantify the EO effect, measurements were performed in free space using a similar setup as described in the work of Abel et al.[26] A r_{eff} was calculated by determining the electric field-induced polarization change of a transmitted laser beam (generated using a 1550 nm fiber coupled laser diode). An interdigitated electrode pattern is defined on the sample using UV-lithography, Ti/Au e-gun deposition, and lift-off. Here, the desired electrode pattern is embedded into the photoresist using a Karl Suss MA6Mask Aligner. A 10 nm Ti film and 400 nm Au film is deposited using a Leybold UNIVEX coating system and lift-off is used to remove regions of unexposed resist. The initial Ti film acts as an adhesive film between the Au and the substrate. Linearly polarized light passes through the $Pb(Zr,Ti)O_3$ film under perpendicular incidence with a polarization direction of 45° with respect to the electrodes. The laser light is first collimated using an aspheric collimator lens and then focused between the electrode with a gap of 10 μm using another aspheric lens. The refractive index change in the $Pb(Zr,Ti)O_3$ film due to the applied electric field causes birefringence of the incident light. After passing through a half-wave plate and polarizer, the transmitted power is proportional to the induced retardation. A modulated signal of V_{mod} = 5V at a frequency of f = 25 kHz was used and the EO response was amplified through a lock-in detection scheme. A schematic representation of the measurement setup can be found in Figure S1 of the Supporting Information (SI). In this setup, the transmitted optical power P_{out} is given by (see SI, eq S6):

$$P_{out} = \left(\frac{1}{2} + \frac{\alpha\pi n^3 r_{eff} t V_{mod}}{2\lambda g}\right) P_{in} \quad (2)$$

where λ is the wavelength of the laser, g is the distance between the electrodes, α a correction factor for the electric field,[27] n is the refractive index, and t is the thickness of the $Pb(Zr,Ti)O_3$ film, V_{mod} is the amplitude of the modulated signal, P_{in} is the incident laser power and r_{eff} the effective Pockels coefficient. The refractive index was calculated with a reflectometry setup using the QE Pro series spectrometer. The correction factor α is used to correct the parallel plate capacitor approximation where $E = V/g$. α is calculated using a

https://doi.org/10.1021/acsami.4c07073
ACS Appl. Mater. Interfaces 2024, 16, 41134–41144

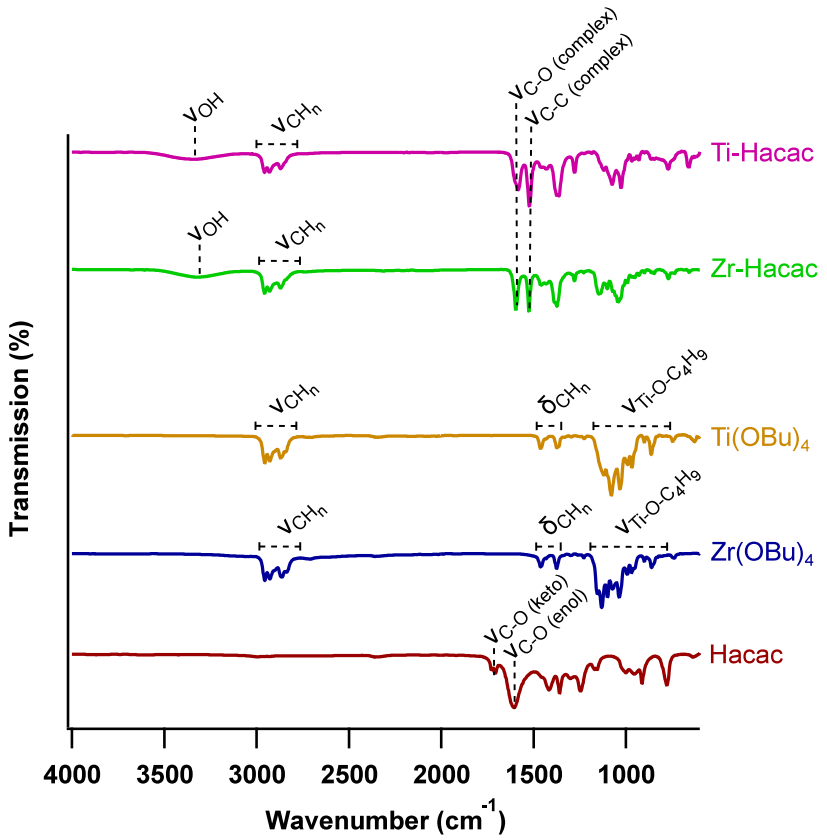

Figure 1. $M(OBu)_4$ (M: Zr,Ti) compound can be complexed with Hacac, leading to the formation of a ring complex. The formation of the ring complex is evidenced by the appearance of the characteristic C−O and C−C bands of the complex and OH band of the formed alcohol in the ATR-FTIR spectrum.

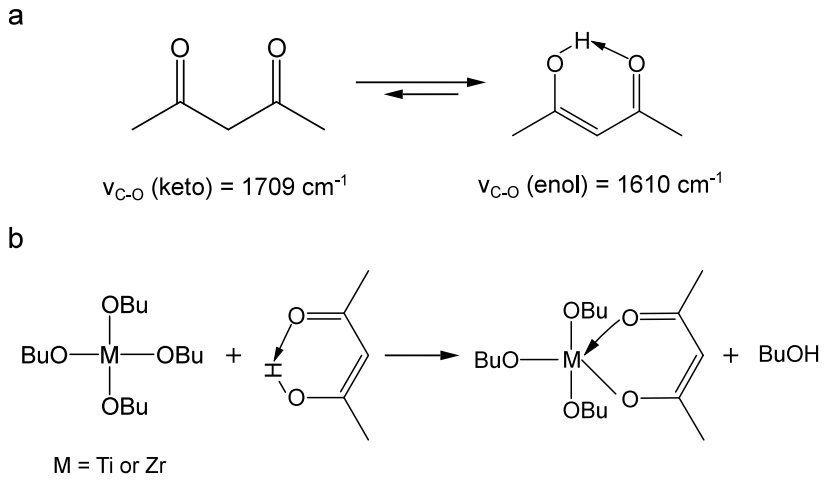

Figure 2. (a) The tautomeric reaction of Hacac leads to two characteristic C−O vibrations (keto−enol). (b) The complexation reaction of $M(OBu)_4$ (M: Zr,Ti) with Hacac (enol form) leads to the formation of a ring structured complex.

finite element solver and defined such that $E = \alpha V/g$. From the aforementioned equation, it is possible to determine the r_{eff} of the $Pb(Zr,Ti)O_3$ thin film. Here, it is not necessary to align the electric field with respect to an in-plane crystal axis, since the polarization of the domains is randomly aligned in-plane due to the fiber texture of the $Pb(Zr,Ti)O_3$ film. Consequently, the EO response of the fiber-textured $Pb(Zr,Ti)O_3$ film is not dependent on the in-plane orientation of the electrode on the sample. Finally, stability over time of the $Pb(Zr,Ti)O_3$ thin film was investigated for 60 h while measurements were taken every minute to calculate the r_{eff}.

Device Fabrication and Characterization. In this work, silicon-nitride (SiN) PICs are designed for two main reasons. First, SiN waveguides could be integrated directly on the $BaTiO_3$ film which minimizes the processing steps. Second, the low refractive index of SiN results in a high optical power confinement in the $Pb(Zr,Ti)O_3$ film. The simulation results of the design are shown in Figures S2 and S3. The $Pb(Zr,Ti)O_3$ film was first deposited on a Si (100) substrate with 3 μm thermally grown SiO_2. A 150 nm thick SiN layer was then deposited on top of a 70 nm thick $Pb(Zr,Ti)O_3$ film using an Advanced Vacuum Vision 310 plasma enhanced chemical vapor deposition (PECVD) system. After deposition, a Raith Voyager

https://doi.org/10.1021/acsami.4c07073
ACS Appl. Mater. Interfaces 2024, 16, 41134−41144

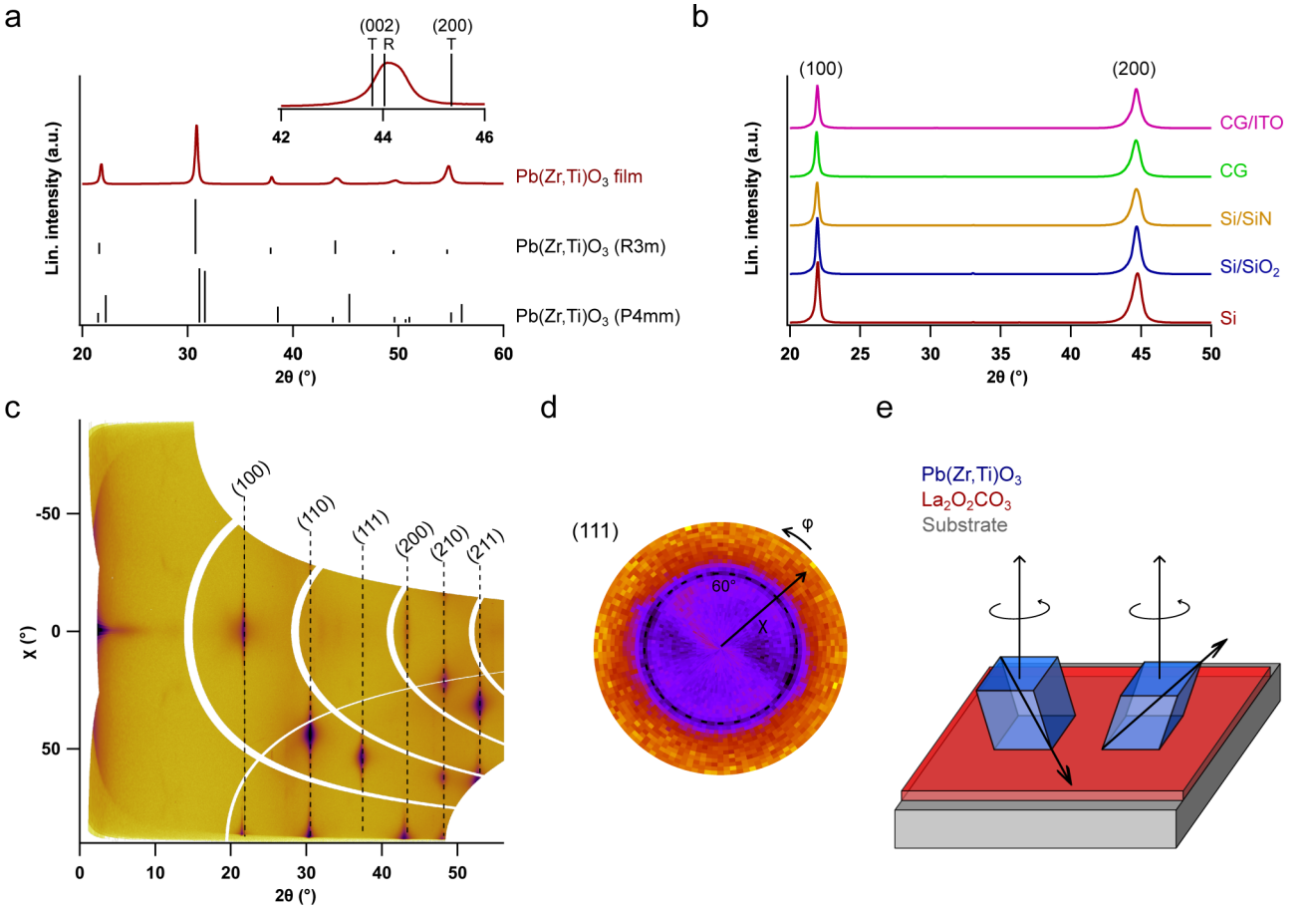

Figure 3. (a) The azimuthally integrated GIWAXS data of the $Pb(Zr,Ti)O_3$ film is compared with the two possible ferroelectric $Pb(Zr,Ti)O_3$ phases (Rhombohedral (PDF: 00−79−2022) and tetragonal (PDF:00−33−0784). The rhombohedral crystal phase is predominant in the $Pb(Zr,Ti)O_3$ film as no peak splitting related to the tetragonal crystal phase is observed (see inset). (b) Out-of-plane θ-2θ XRD measurements of integrated $Pb(Zr,Ti)O_3$ films on different substrates. A film with strong out-of-plane preferential orientation is present on all substrates. (c) 2D GIWAXS image showing the strong preferential out-of-plane orientation of the $Pb(Zr,Ti)O_3$ film (d) No preferred in-plane orientation is present as a circle is observed in the pole figure measurement of the (111) plane. (e) Illustration of the orientation of the predominant rhombohedral phase yields both an in-plane and out-of-plane polarization component.

Electron Beam Lithography (EBL) system was used to pattern the designs onto the photonic chip. The designs were then etched into the SiN layer using an Advanced Vacuum Vision 320 reactive ion etcher (RIE). Finally, electrode patterns were defined on the sample using UV-lithography, Ti/Au e-gun deposition, and lift-off. A graphical representation of the device cross-section is shown in Figure S4. The DC operation of the $Pb(Zr,Ti)O_3$ film was investigated using a SiN O-band ring resonator with a simple benchtop measurement setup. A tunable TSL-510 O-band laser from Santec was used to generate light at a wavelength of 1310 nm. This light was coupled into and out of the photonic chip via grating couplers specifically designed for this film stack and wavelength (Figures S5 and S6). The transmitted light was recorded using a Newport 1936-R optical power meter. A Keithley 2400 Standard Series source measure unit (SMU) and MPI coaxial DC probes were used to contact and apply voltages to the Au electrodes on the ring resonator.

RESULTS AND DISCUSSION

Improving Ink Stability by Complexing the M-Alkoxides (M:Ti,Zr). The formulation of a stable and homogeneous precursor solution is an essential prerequisite for the preparation of high-quality $Pb(Zr,Ti)O_3$ thin films by the CSD process. Therefore, the inherent hydrolysis reactions of Zr and Ti alkoxides, which can lead to precipitation products and/or inhomogeneous solutions, must be counteracted. For this reason, β-diketones are added to the solution because they react readily with the Zr and Ti alkoxides and form less hydrolyzable complexes due to the steric effect of the complex compound. In this way, the precursor solution can be stabilized for more than 5 months without precipitation.[28,29] The formation of these complexes is confirmed by ATR-FTIR and is shown in Figure 1. Here, actylacetone (Hacac) is used as the β-diketone.

In the ATR-FTIR spectra, the characteristic bands for Hacac (ν = 1709 and 1610 cm^{-1}) are associated with the C═O stretching vibration of the keto form and the HO−C═C stretching vibration of the enolic form conjugated to C═O, respectively.[30−32] An illustration of the two different tautomeric forms is shown in Figure 2a. For $Zr(OBu)_4$ and $Ti(OBu)_4$, the characteristic bands in the high frequency region (ν = 2956 cm^{-1}, 2930 cm^{-1}, and 2870 cm^{-1}; δ = 1460 cm^{-1}, 1374 cm^{-1}) correspond to the stretching and bending vibrations of the alkyl groups (CH_2 and CH_3). In the low-frequency region of the spectrum (below 1150 cm^{-1}), the series of bands corresponds to the Ti−O-R stretching vibrations of OC_4H_9 groups bound directly to Ti.[33,34] For the $M(OBu)_4$ (M: Zr,Ti)-Hacac mixture, complex formation is supported by the appearance of two new characteristic bands

https://doi.org/10.1021/acsami.4c07073
ACS Appl. Mater. Interfaces 2024, 16, 41134−41144

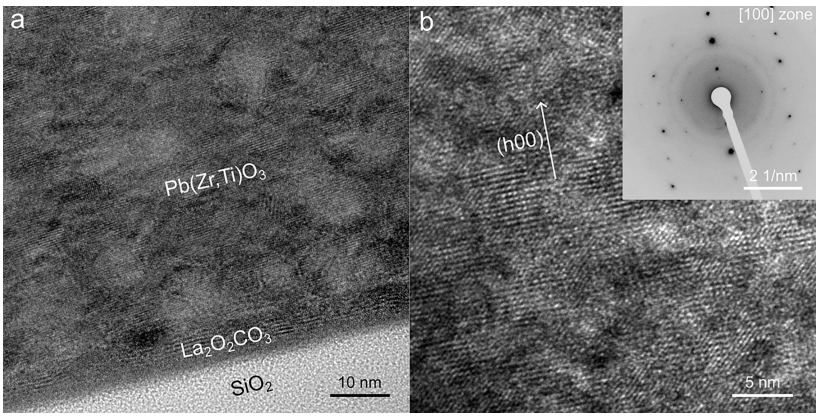

Figure 4. (a) HRTEM image of a $La_2O_2CO_3/Pb(Zr,Ti)O_3$ stack integrated on a Si/SiO_2 substrate showing both a highly crystalline $La_2O_2CO_3$ and $Pb(Zr,Ti)O_3$ thin film. (b) HRTEM image and SAEDP analysis of the $Pb(Zr,Ti)O_3$ film showing the preferred out-of-plane orientation of the $Pb(Zr,Ti)O_3$ thin film.

(ν = 1590 and 1522 cm^{-1}) associated with the C−O and C−C stretching vibrations in the ring complexes formed.[35−37] The ring complexes are formed by the reaction of the enol form of Hacac with the $M(OBu)_4$ (M:Zr,Ti), as shown in Figure 2b. An additional indication of this complexation reaction is the appearance of the broad OH vibration (ν = 3364 cm^{-1}) in the spectrum. Moreover, the disappearance of the characteristic Hacac-related bands indicates that all the Hacac molecules are consumed and both the Ti and Zr ions are fully complexed, since the molar ratio of Hacac/$M(OBu)_4$ (M:Zr,Ti) is 1:1. Thus, in the course of the reaction, the keto form is converted to the enol form, which eventually reacts completely. Since the other characteristic bands of Hacac and $M(OBu)_4$ (M:Zr,Ti) compounds are not involved in the complexation reaction, they are nevertheless present in the spectrum of M (M:Zr,Ti)-Hacac. In addition to the appearance of the characteristic bands in the spectrum, the formation of the ring complex can also be observed visually, as the formation of the ring complex is responsible for the yellowish color in solution.[38]

Microstructural Characterization of the $Pb(Zr,Ti)O_3$ Film. The electro-optic properties of the $Pb(Zr,Ti)O_3$ film are closely related to its crystal phase and film texture. Therefore, these structural properties should be determined first. Since the Zr/Ti ratio (52/48) in our precursor solution was set to fulfill the morphotropic phase boundary condition (MPB), two ferroelectric phases of the $Pb(Zr,Ti)O_3$ film could potentially form: rhombohedral ($R3m$) and/or tetragonal ($P4mm$).[23,39,40] To determine the formed phase(s) in solution processed $Pb(Zr,Ti)_3$ film, the azimuthal integration of the 2D GIWAXS images of the $Pb(Zr,Ti)O_3$ film is compared with the corresponding simulated powder diffraction files (PDFs): rhombohedral (PDF: 00−73−2022) and tetragonal (PDF: 00−33−0784). However, since the lattice parameters of the $Pb(Zr,Ti)O_3$ phases strongly depend on the precursors, the synthesis method and the Zr/Ti ratio,[41] the lattice parameters of both phases are first refined using a Pawley fit on pure rhombohedral (70/30) and tetragonal (30/70) calcined $Pb(Zr,Ti)O_3$ powders.[41] In this way, more representative lattice parameters are obtained for our solution processing method. The powders were calcined using the same thermal annealing process as the films. The Pawley fittings and the refined lattice parameters are shown in Figure S7 and Table S1. Consequently, the simulated PDFs can be compared with the azimuthal integration of the $Pb(Zr,Ti)O_3$ film as shown in Figure 3a. Here, a good agreement with the rhombohedral phase can be observed, as the characteristic peak splitting (e.g., (200)/(002)) of the tetragonal phase is not present (see inset). In the case of the rhombohedral phase, the elongation of the unit cell occurs along the [111] direction, which does not cause a splitting of the (200) peak.[41−43] Consequently, the GIWAXS data of the $Pb(Zr,Ti)O_3$ film indicate the main formation of the rhombohedral phase, but it should be noted that the coexistence of a small fraction of the tetragonal phase is not excluded, as a small peak shift and broadening of the (200) peak is also observed. It is therefore most likely that a mixture of the two phases is present, with the rhombohedral phase being the predominant ferroelectric phase.

In addition to the preferred rhombohedral phase formation, the $Pb(Zr,Ti)O_3$ films also exhibit a high degree of texture. In Figure 3b, out-of-plane θ-2θ measurements of the $Pb(Zr,Ti)O_3$ film integrated on different substrates (Si, Si/SiO_2, Si/SiN, corning glass (CG), and CG/ITO) show only strong (h00) reflections. Consequently, the $Pb(Zr,Ti)O_3$ film has a preferred (h00) out-of-plane orientation that is not influenced by the type of substrate. This preferred orientation is caused by the $La_2O_2CO_3$ template film, which acts as a self-orienting template film that is compatible with both crystalline and amorphous substrates.[20] The preferential (h00) out-of-plane orientation of the $Pb(Zr,Ti)O_3$ film is quantitatively expressed by a calculated LF value of 0.999 (see Experimental Section). This almost perfect (h00) out-of-plane orientation is also shown in the 2D GIWAXS image of the film in Figure 3c. Here it can be seen that very clear peaks only occur at the specific χ angles, as the presence of randomly oriented grains would contribute to the formation of vertical lines in the image. Consequently, the $Pb(Zr,Ti)O_3$ films exhibit a very strong (h00) out-of-plane preferred orientation.

To evaluate the in-plane orientation of the film, a pole figure measurement of the (111) plane at 2θ = 38.893° of the $Pb(Zr,Ti)O_3$ film was performed and shown in Figure 3d. Here, a ring are observed at χ = 60°, indicating that there is no preferred in-plane orientation, which is consistent with the corresponding fiber texture orientation of the $La_2O_2CO_3$ template film.[20] In other words, the $Pb(Zr,Ti)O_3$ film mainly has a rhombohedral phase, can be integrated on various substrates and has a fiber texture. Since the polar axis of the unit cell runs along the [111] direction, this results in both an in-plane and an out-of-plane polarization component in the

https://doi.org/10.1021/acsami.4c07073
ACS Appl. Mater. Interfaces 2024, 16, 41134−41144

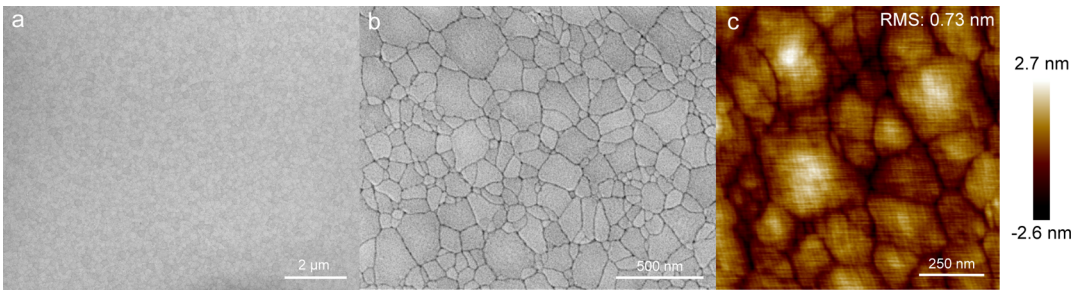

Figure 5. Surface analysis by SEM and AFM shows that the ferroelectric stack has a dense microstructure (a,b) and a low surface roughness (RMS of 0.73 nm) for a 65 nm thick $Pb(Zr,Ti)O_3$ film.

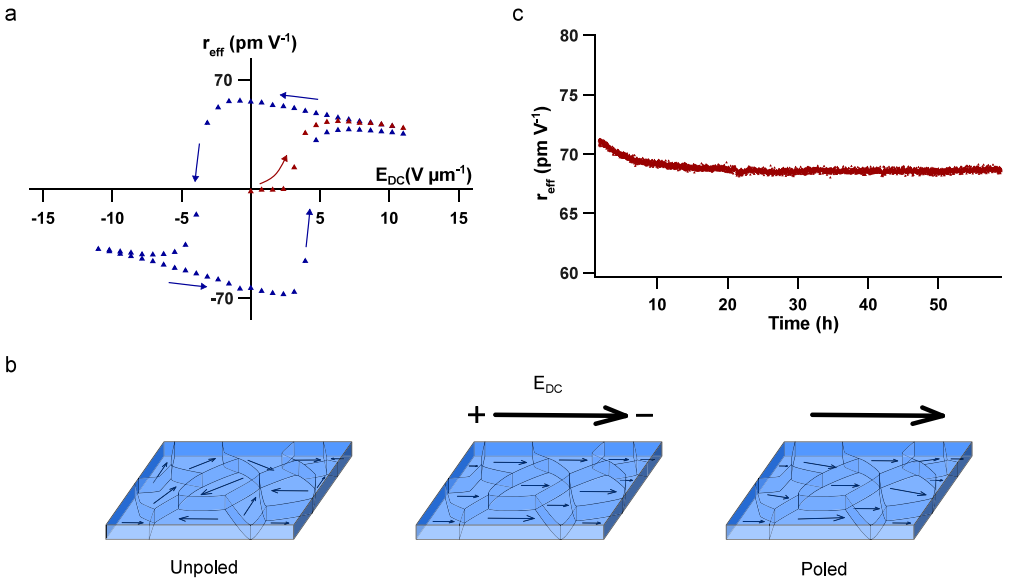

Figure 6. (a) The $Pb(Zr,Ti)O_3$ exhibits a hysteresis loop after poling, as expected due to the reorientation of the in-plane polarization domains as the field is swept back and forth. (b) Graphical illustration of the reorientation of the averaged in-plane polarization in a grain by applying an electric field. The averaged in-plane polarization is a summation of the individual dipole moments of the rhomboedral and tetragonal unit cells present in a grain (c) A large remnant r_{eff} remains present in the film and is stable over a long time.

$Pb(Zr,Ti)O_3$ unit cell, as shown in Figure 3e. However, the polar axis can also be aligned along the in-plane mirrored $[11\bar{1}]$, resulting in no net in-plane or out-of-plane polarization in the absence of an electric field.

In addition to structural characterization by X-ray diffraction, the highly textured $Pb(Zr,Ti)O_3$ film is also visualized by HRTEM, as shown in Figure 4a, b. Here, the integration of a highly crystalline $Pb(Zr,Ti)O_3$ film on a Si/SiO_2 substrate using the $La_2O_2CO_3$ template film is confirmed. In addition, the $La_2O_2CO_3$ film itself still shows its characteristic layer-like structure, indicating the stability of the template film up to a temperature of at least 600 °C.[14,20] On the high magnification image (Figure 4b), the preferred out-of-plane orientation of the $Pb(Zr,Ti)O_3$ film is clearly visible, which is also confirmed by the analysis of the selected area electron diffraction pattern (SAEDP) (see inset).

In addition to the structural properties, low surface roughness is also an important prerequisite for the production and integration of high-quality electro-optically active $Pb(Zr,Ti)O_3$ films, as this can contribute significantly to propagation losses as a scattering source.[44] Figure 5a shows planar-view SEM of the $Pb(Zr,Ti)O_3$ film. The surface morphology of the films is dense and smooth and exhibits a microstructure characteristic of the material. Typical columnar grains with a diameter of 20−350 nm and an estimated mean value of 117 nm are observed.[14,45,46] The roughness of the film was quantified by surface analysis using AFM (Figure 5b) and yielded a RMS roughness value of 0.73 nm for a 65 nm thick $Pb(Zr,Ti)O_3$ film. This value is comparable or lower than for other $Pb(Zr,Ti)O_3$ films.[47−49]

Determination of the Pockels Coefficient of the $Pb(Zr,Ti)O_3$ film. Before determining the EO properties, it is important to evaluate the electrical properties. Electrical characterization has been performed on a CG-ITO sample with round dots of a Au top electrode. Measurement results of the complex impedance and the hysteresis loop can be found in Figures S10 and S11 respectively, demonstrating excellent ferroelectric properties. Subsequently, EO measurements are performed and the Pockels coefficient is calculated using eq 2 in the Experimental Section. Since the optical power is mapped linearly to a voltage through the photodetector, eq 2 can be expressed in terms of the photodetector voltage V_{PD}. If we now consider the change in the photodetector voltage due to a modulation voltage (i.e., we take the derivative after the modulation voltage V_{mod}), then we obtain the following expression (see SI, eq S10):

https://doi.org/10.1021/acsami.4c07073
ACS Appl. Mater. Interfaces 2024, 16, 41134−41144

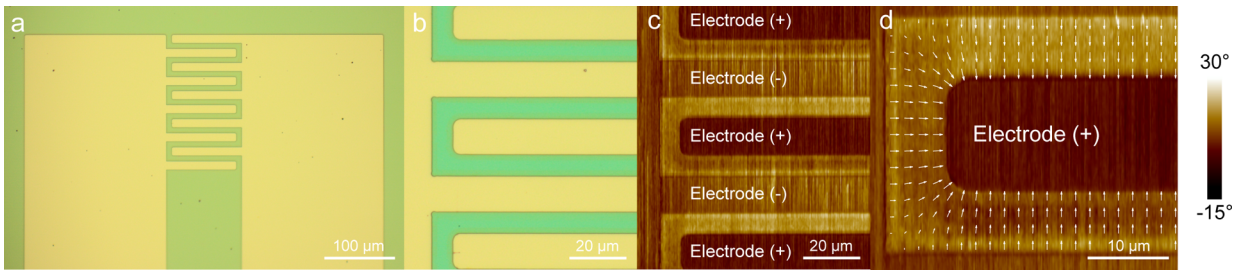

Figure 7. (a,b) Microscopic images of the IDTs fabricated on the $Pb(Zr,Ti)O_3$ film. (c) The remnant polarization is evident from the phase measurement of a selected ROI of the IDTs. (d) The phase measurement around an electrode is overlaid with a quiver plot of the electric field distribution to further visualize the realignment of the ferroelectric domains.

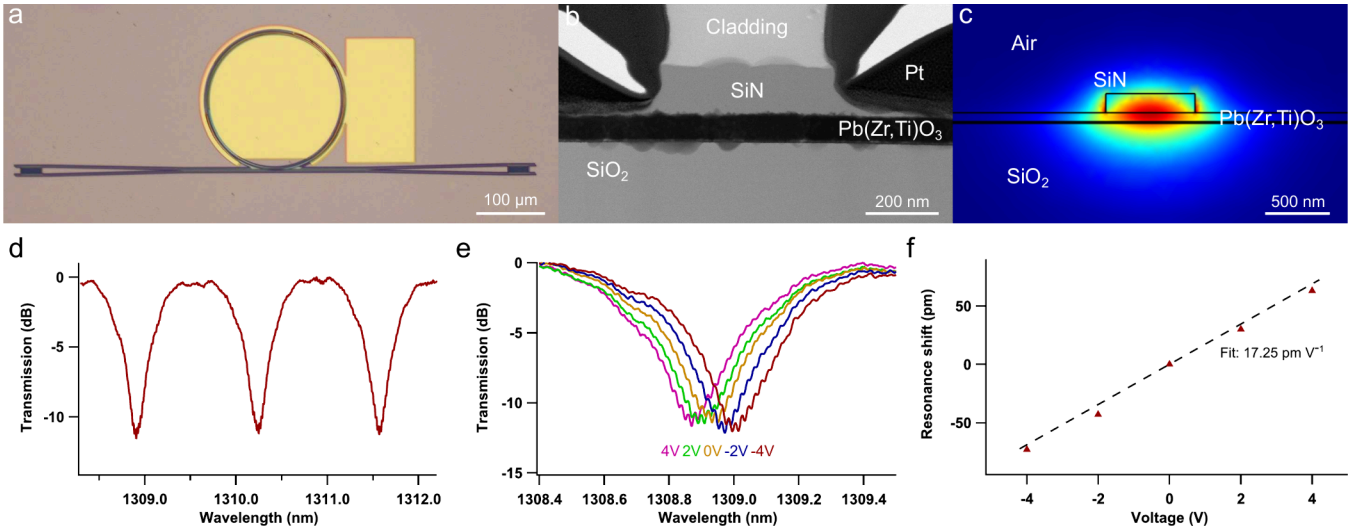

Figure 8. Design and response of a O-band ring modulator. (a) Top view of the SiN waveguides fabricated on the $Pb(Zr,Ti)O_3$ film. (b) Cross-sectional TEM view of the SiN waveguide on the $Pb(Zr,Ti)O_3$ film. Note: The $La_2O_2CO_3$ film (7 nm) is not visible at this magnification. (c) Simulation of the TE optical mode in the waveguide structure.(d) Normalized transmission spectrum of the O-band ring modulator with a $\Delta\lambda_{FSR}$ of 1.33 nm (e) The normalized transmission spectra for different DC voltages. (f) The resonance wavelength shift in function of the applied voltage across the $Pb(Zr,Ti)O_3$ film shows the expected linear trend with a tuning efficiency of 17.25 pm V^{-1}.

$$r_{\text{eff}} = \frac{\lambda g}{\alpha n^3 \pi t V_{\text{PD}}} \frac{\partial V_{\text{PD},0}}{\partial V_{\text{mod}}} \tag{3}$$

where λ (1550 nm) is the wavelength of the laser, g (10 μm) is the distance between the electrodes, α (0.905) is a correction term for the electric field (see Experimental Section),[27] n (2.4) is the refractive index, t (200 nm) is the thickness of the film, $V_{\text{PD},0}$ (V) is the photodetector voltage, and $\partial V_{\text{PD}}/\partial V_{\text{mod}}$ is the change in photodetector voltage due to the modulated signal.

The calculated r_{eff} of the $Pb(Zr,Ti)O_3$ film as a function of an external DC bias field ($E_{\text{DC}} = V/g$) is shown in Figure 6a (raw data can be found in Figure S8). Initially, the unpoled $Pb(Zr,Ti)O_3$ film shows almost no EO response because the polarization domains are randomly oriented in-plane and the responses of two antiparallel domains cancel each other out. An increase in E_{DC} leads to a strong increase in r_{eff}, which results from the realignment of the in-plane polarization domains, eliminating antiparallel domains. Finally, all polarization domains are maximally aligned with the applied electric field component and the r_{eff} is saturated. An overview of a possible domain realignment process is shown in Figure 6b. Here, only the in-plane polarization component is shown as the out-of-plane component will be canceled out as it is equally likely to have its polar axis along the [111] as well as the in-plane mirrored $[11\bar{1}]$ resulting in a net zero-out-of-plane polarization. Therefore, the reorientation process is graphically represented by the averaged in-plane polarization (arrow) in a grain, which is an averaging of the individual in-plane dipole moment present in each unit cell. The individual rhombohedral unit cell, can rotate its polar axis by 90° or 180° to maximize the alignment of its electric dipole with the applied field, leading to a maximization of the averaged in-plane polarization in a grain. Once the sample is fully poled, a symmetrical hysteresis loop is monitored during a full sweep of E_{DC}, which is a clear signature of the ferroelectric nature of the stack.[50,51] To evaluate the average maximum and remnant EO response of the $Pb(Zr,Ti)O_3$ film, different electrode pads were measured and the measurements were performed several times per pad. This resulted in an average maximum r_{eff} of 68.98 pm V^{-1} ∓ 4.98 and a remnant r_{eff} coefficient of 65.95 pm V^{-1} ∓ 5.83, whereby the specified error is a standard deviation. The error is due to small variations in processing conditions, including electrode spacing and thickness variations. Here, it is clear that after poling a very strong remnant polarization is present as the remnant EO response is almost similar to the maximum EO response. The decreasing slope at large—E_{DC}—values is most likely related to nonlinear EO effects,[26] piezoelectric effects and/or charge accumulation at the electrode interface. In addition, a large coercive field of E_c = 4.7 V μm^{-1} is derived from the shape of the hysteresis, which is

https://doi.org/10.1021/acsami.4c07073
ACS Appl. Mater. Interfaces 2024, 16, 41134−41144

consistent with other $Pb(Zr,Ti)O_3$ thin films.[27,52,53] Furthermore, the stability of the remnant EO response over time was evaluated and shown in Figure 6c. Apart from small changes in the first hours, which are related to transient phenomena regarding ferroelectric domain reorientation, the remnant r_{eff} is very stable over time.

Furthermore, the stability of the ferroelectric domains allows the visualization of the domain orientation by PFM measurements after poling. Figure 7a shows a photo of the IDT electrodes (10 μm spacing) used to polarize the $Pb(Zr,Ti)O_3$ intermediate domains (10 V for 10 min). Subsequently, PFM measurements are performed on a smaller region of interest (ROI) (Figure 7b), and the PFM phase shift in this ROI is shown in Figure 7c. Here it is clear that the intervening $Pb(Zr,Ti)O_3$ regions between two IDT electrodes exhibit a different phase shift caused by the opposite poling direction. To visualize the realignment of the ferroelectric domains, the phase shift around an IDT is overlaid with a quiver plot of the electric field distribution, as shown in Figure 7d. Here, the gradient along the corners of the electrode clearly shows the realignment of the domains in the $Pb(Zr,Ti)O_3$ thin films. The color difference near the edges of the electrode is due to the residues remaining after lift-off and is not related with the realignment of the ferroelectric domains.

Integration of the $Pb(Zr,Ti)O_3$ Film into a SiN Ring Resonator. To validate the operation in functional devices, a $Pb(Zr,Ti)O_3$ film is integrated into a SiN O-band ring resonator (see Experimental Section). Figure 8a,b shows the top view of a ring resonator with coplanar gold electrode pads and the waveguide cross-section. Since the polarization domains in the $Pb(Zr,Ti)O_3$ films are randomly oriented in-plane, the distribution of the polarization domains will be uniform along the ring resonator circumference, which means that it is possible to deposit electrodes along its entire circumference. Light with a wavelength centered around 1310 nm is coupled into the fundamental quasi-transverse electric (quasi-TE) optical mode. A simulation of this quasi-TE mode is shown in Figure 8c, which shows that a significant fraction (29.83%) of the optical mode is confined in the $Pb(Zr,Ti)O_3$ film (Figure S9). The transmission spectrum of the O-band ring modulator is shown in Figure 8d. The $Pb(Zr,Ti)_3$ is first poled using a voltage of 50 V (8.33 V μm^{-1}) for 10 min. Then the Pockels effect is measured using small variations of the electric field of maximum one tenth of the poling voltage to make sure the domains are not repoled. The small electric field causes a refractive index shift in the $Pb(Zr,Ti)O_3$ film (eq 1), changing the resonant wavelength of the ring resonator and turning it into a functional EO modulator. In Figure 8e, the shift of the resonance wavelength is plotted as a function of the applied voltage. The tuning efficiency is now calculated as the slope of the wavelength shift due to the applied voltage $\Delta\lambda/\Delta V$, which is shown in Figure 8f. This plot shows a linear trend (R = 0.9968) as all polarization domains are maximally aligned after poling with a tuning efficiency of $\Delta\lambda/\Delta V$ = 17.25 pm V^{-1}. This tuning efficiency is then used to determine the half-wave voltage-length product, which is defined as follows

$$V_\pi L = \frac{L\lambda_{FSR}\Delta V}{2\Delta\lambda} \tag{4}$$

where L (524 μm) is the length of the phase shifter, λ_{FSR} (1.33 nm) is the free spectral range and $\Delta\lambda/\Delta V$ (pm V^{-1}) is the tuning efficiency of the ring. From the half-wave voltage-length product it is possible to calculate the Pockels coefficient responsible for the phase tuning in the waveguide structure r_{wg}, using eq 5. Note that this is not the same Pockels coefficient as mentioned in eq 3, as the alignment of the electrical field and polarization of the light is different. Here, the polarization of the light coupled into the waveguide is a TE mode and is parallel to the electric field.

$$r_{wg} = \frac{\lambda g}{\Gamma n^3 V_\pi L} \tag{5}$$

where λ (1310 nm) is the wavelength, g (6 μm) is the distance between the electrodes, n (2.4) the refractive index of the $Pb(Zr,Ti)O_3$ film, Γ (0.298) the electro-optic overlap integral (eq S11) and the $V_\pi L$ half-wave voltage-length product of the ring.[21] Using the results from Figure 8e, a half-wave voltage-length product of $V_\pi L$ = 2.019 V cm and r_{wg} = 94.50 pm V^{-1} are obtained, yielding comparable results to those reported in state-of-the-art $Pb(Zr,Ti)O_3$ thin films.[13,54] In addition, the poling is stable and there have been no indications of decay of much longer periods of time.

CONCLUSIONS

In summary, we have determined the EO properties of the fabricated solution processed $Pb(Zr,Ti)O_3$ films. For this purpose, a stable $Pb(Zr,Ti)O_3$ (52/48) precursor solution is obtained by a complexation reaction with Hacac. The $Pb(Zr,Ti)O_3$ film exhibits a characteristic microstructure, low surface roughness (RMS = 0.73 nm) and a predominant rhombohedral crystal phase ($R3m$). Since the polar axis is along the [111] direction, both an in-plane and an out-of-plane polarization component are present in the unit cell. This results in a large remnant r_{eff} of 65.95 pm $V^{-1} \mp$ 5.83 and a maximized r_{eff} of 68.98 pm $V^{-1} \mp$ 4.98. Furthermore, the $Pb(Zr,Ti)O_3$ film is integrated into a SiN ring resonator and has a $V_\pi L$ of 2.019 V cm and r_{wg} of 94.50 pm V^{-1}. Consequently, we have proposed a solution-based fabrication method for $Pb(Zr,Ti)O_3$ thin films that yields a high maximum r_{eff} and a high remnant r_{eff}. In this way, cost-efficient, high-throughput and flexible integration of $Pb(Zr,Ti)O_3$ films for Si photonics is possible, providing an opportunity to increase the applicability of $Pb(Zr,Ti)O_3$ thin films for EO applications in the future.

ASSOCIATED CONTENT

Supporting Information

The Supporting Information is available free of charge at https://pubs.acs.org/doi/10.1021/acsami.4c07073.

Schematic of the EO transmission setup in free space, derivation of the transmitted optical power and Pockels coefficient in the EO free space setup, determination of single mode waveguide width for SiN platform, electrical and optical field overlap calculation, a graphical representation of the device cross-section, grating coupler design for SiN platform, Pawley fittings on the ferroelectric $Pb(Zr,Ti)O_3$ phases (Zr/Ti): Rhombedral (70/30) and tetragonal (30/70), raw data of EO transmission setup, calculation EO overlap integral, and electical characterization of the thin films (PDF)

https://doi.org/10.1021/acsami.4c07073
ACS Appl. Mater. Interfaces 2024, 16, 41134−41144

AUTHOR INFORMATION

Corresponding Authors

Klaartje De Buysser − *SCRiPTS, Department of Chemistry, Ghent University, 9000 Ghent, Belgium;* orcid.org/0000-0001-7462-2484; Email: klaartje.debuysser@ugent.be

Jeroen Beeckman − *LCP Group, Department of Electronics and Information Systems, Ghent University, 9052 Gent, Belgium;* orcid.org/0000-0002-0711-2465; Email: jeroen.beeckman@ugent.be

Authors

Ewout Picavet − *SCRiPTS, Department of Chemistry, Ghent University, 9000 Ghent, Belgium; LCP Group, Department of Electronics and Information Systems, Ghent University, 9052 Gent, Belgium*

Kobe De Geest − *LCP Group, Department of Electronics and Information Systems, Ghent University, 9052 Gent, Belgium; PRG, Department of Information Technology, Ghent University-IMEC, 9052 Gent, Belgium;* orcid.org/0000-0002-5669-975X

Enes Lievens − *LCP Group, Department of Electronics and Information Systems, Ghent University, 9052 Gent, Belgium; PRG, Department of Information Technology, Ghent University-IMEC, 9052 Gent, Belgium*

Hannes Rijckaert − *SCRiPTS, Department of Chemistry, Ghent University, 9000 Ghent, Belgium; LCP Group, Department of Electronics and Information Systems, Ghent University, 9052 Gent, Belgium;* orcid.org/0000-0002-6078-2919

Tom Vandekerckhove − *LCP Group, Department of Electronics and Information Systems, Ghent University, 9052 Gent, Belgium;* orcid.org/0000-0002-5639-9300

Eduardo Solano − *NCD-SWEET beamline, ALBA Synchrotron Light Source, 08290 Cerdanyola del Valles, Spain;* orcid.org/0000-0002-2348-2271

Davy Deduytsche − *CoCooN Group, Department of Solid State Sciences, Ghent University, 9000 Ghent, Belgium*

Laura Van Bossele − *SCRiPTS, Department of Chemistry, Ghent University, 9000 Ghent, Belgium; LCP Group, Department of Electronics and Information Systems, Ghent University, 9052 Gent, Belgium;* orcid.org/0000-0003-3016-2927

Dries Van Thourhout − *PRG, Department of Information Technology, Ghent University-IMEC, 9052 Gent, Belgium;* orcid.org/0000-0003-0111-431X

Complete contact information is available at: https://pubs.acs.org/10.1021/acsami.4c07073

Notes

The authors declare no competing financial interest.

ACKNOWLEDGMENTS

GIWAXS experiments were recorded at NCD-SWEET beamline at ALBA synchrotron with collaboration of ALBA staff. TEM measurements were performed by Hannes Rijckaert at the UGent TEM Core Facility. E.P. acknowledges support and funding as an SB-PhD Fellow of the Research Foundation−Flanders (FWO, Grant number 3S041219). Electrical characterization was performed by Jiayi Liu. H.R. acknowledges support and funding as postdoctoral fellow fundamental research of the Research Foundation−Flanders (FWO, Grant number 1273621N). This work was financially supported by Special Research Fund - UGent (BOF20/GOA/027) and the Horizon Europe project VISSION (Grant ID: 101070622).

REFERENCES

(1) Smith, G. L.; Pulskamp, J. S.; Sanchez, L. M.; Potrepka, D. M.; Proie, R. M.; Ivanov, T. G.; Rudy, R. Q.; Nothwang, W. D.; Bedair, S. S.; Meyer, C. D.; Polcawich, R. G. others PZT-based Piezoelectric MEMS Technology. *J. Am. Ceram. Soc.* **2012**, *95*, 1777−1792.

(2) Muralt, P. Recent Progress in Materials Issues for Piezoelectric MEMS. *J. Am. Ceram. Soc.* **2008**, *91*, 1385−1396.

(3) Lee, B.; Lin, S.; Wu, W.; Wang, X.; Chang, P.; Lee, C. Piezoelectric MEMS Generators Fabricated with an Aerosol Deposition PZT Thin Film. *Journal of Micromechanics and Microengineering* **2009**, *19*, No. 065014.

(4) Brennecka, G. L.; Ihlefeld, J. F.; Maria, J.-P.; Tuttle, B. A.; Clem, P. G. Processing Technologies for High-permittivity Thin Films in Capacitor Applications. *J. Am. Ceram. Soc.* **2010**, *93*, 3935−3954.

(5) Palneedi, H.; Peddigari, M.; Hwang, G.-T.; Jeong, D.-Y.; Ryu, J. High-performance Dielectric Ceramic Films for Energy Storage Capacitors: Progress and Outlook. *Adv. Funct. Mater.* **2018**, *28*, 1803665.

(6) Ramesh, R.; Aggarwal, S.; Auciello, O. Science and Technology of Ferroelectric Films and Heterostructures for Non-volatile Ferroelectric Memories. *Materials Science and Engineering: R: Reports* **2001**, *32*, 191−236.

(7) Morioka, H.; Asano, G.; Oikawa, T.; Funakubo, H.; Saito, K. Large Remanent Polarization of 100% Polar-axis-oriented Epitaxial Tetragonal Pb $(Zr_{0.35}Ti_{0.65})O_3$ Thin Films. *Applied physics letters* **2003**, *82*, 4761−4763.

(8) Lee, H. N.; Nakhmanson, S. M.; Chisholm, M. F.; Christen, H. M.; Rabe, K. M.; Vanderbilt, D. Suppressed Dependence of Polarization on Epitaxial Strain in Highly Polar Ferroelectrics. *Physical review letters* **2007**, *98*, 217602.

(9) Fang, Z.; Chen, R.; Tossoun, B.; Cheung, S.; Liang, D.; Majumdar, A. Non-volatile Materials for Programmable Photonics. *APL Mater.* **2023**, *11*, 100603.

(10) Wen, Y.; Chen, H.; Wu, Z.; Li, W.; Zhang, Y. Fabrication and Photonic Applications of Si-integrated $LiNbO_3$ and $BaTiO_3$ Ferroelectric Thin Films. *APL Mater.* **2024**, *12*, No. 020601.

(11) Cheng, J.; Meng, Z.; Cross, L. E. Piezoelectric PZT Thin Films Derived by Sol-gel Techniques. *Fifth International Conference on Thin Film Physics and Applications*; Shanghai, P.R. China, 2004; pp 124−129.

(12) Zhu, M.; Du, Z.; Jing, L.; Yoong Tok, A. I.; Tong Teo, E. H. Optical and Electro-optic Anisotropy of Epitaxial PZT Thin Films. *Appl. Phys. Lett.* **2015**, *107*, No. 031907.

(13) Ban, D.; Liu, G.; Yu, H.; Sun, X.; Deng, N.; Qiu, F. High Electro-optic Coefficient Lead Zirconate Titanate Films Toward Low-power and Compact Modulators. *Optical Materials Express* **2021**, *11*, 1733−1741.

(14) George, J.; Smet, P.; Botterman, J.; Bliznuk, V.; Woestenborghs, W.; Van Thourhout, D.; Neyts, K.; Beeckman, J. Lanthanide-assisted Deposition of Strongly Electro-optic PZT Thin Films on Silicon: Toward Integrated Active Nanophotonic Devices. *ACS Appl. Mater. Interfaces* **2015**, *7*, 13350−13359.

(15) Bi, Z.; Zhang, Z.; Fan, P. Characterization of PZT Ferroelectric Thin Films by RF-magnetron Sputtering. *Journal of Physics: Conference Series.* **2007**, *61*, 120.

(16) Selvaraja, S. K.; et al. Highly Oriented PZT Films on MgO (002) Platform for Polarization Independent Electro-Optic Modulation. *Photonic Networks and Devices*; 2023; pp JTu4A−12.

(17) Tsuchiya, K.; Kitagawa, T.; Nakamachi, E. Development of RF Magnetron Sputtering Method to Fabricate PZT Thin Film Actuator. *Precision engineering* **2003**, *27*, 258−264.

(18) Pandey, S.; James, A.; Prakash, C.; Goel, T.; Zimik, K. Electrical Properties of PZT Thin Films Grown by Sol−gel and PLD using a Seed Layer. *Materials Science and Engineering: B* **2004**, *112*, 96−100.

(19) Gaidi, M.; Amassian, A.; Chaker, M.; Kulishov, M.; Martinu, L. Pulsed Laser Deposition of PLZT Films: Structural and Optical Characterization. *Appl. Surf. Sci.* **2004**, *226*, 347−354.
(20) Picavet, E.; Rijckaert, H.; Solano, E.; Bikondoa, O.; Fernandez, E. G.; Paturi, P.; Van Bossele, L.; Vrielinck, H.; Beeckman, J.; De Buysser, K. The Self Out-of-plane Oriented $La_2O_2CO_3$ Film: An Integration Tool for Fiber Textured Ferroelectric Thin Films. *J. Mater. Chem. C* **2023**, *11*, 7705−7713.
(21) Alexander, K.; George, J. P.; Verbist, J.; Neyts, K.; Kuyken, B.; Van Thourhout, D.; Beeckman, J. Nanophotonic Pockels Modulators on a Silicon Nitride Platform. *Nat. Commun.* **2018**, *9*, 1−6.
(22) Zhu, M.; Zhang, H.; Du, Z.; Liu, C. Structural Insight into the Optical and Electro-optic Properties of Lead Zirconate Titanate for High-performance Photonic Devices. *Ceram. Int.* **2019**, *45*, 22324−22330.
(23) Mishra, S.; Pandey, D.; Singh, A. P. Effect of Phase Coexistence at Morphotropic Phase Boundary on the Properties of $Pb(Zr_xTi_{1-x})O_3$ Ceramics. *Appl. Phys. Lett.* **1996**, *69*, 1707−1709.
(24) Singh, A.; Mishra, S.; Pandey, D.; Prasad, C. D.; Lal, R. Low-temperature Synthesis of Chemically Homogeneous Lead Zirconate Titanate (PZT) Powders by a Semi-wet Method. *J. Mater. Sci.* **1993**, *28*, 5050−5055.
(25) Furushima, R.; Tanaka, S.; Kato, Z.; Uematsu, K. Orientation Distribution−Lotgering Factor Relationship in a Polycrystalline Material as an Example of Bismuth Titanate Prepared by a Magnetic Field. *Journal of the Ceramic Society of Japan* **2010**, *118*, 921−926.
(26) Abel, S.; Stoferle, T.; Marchiori, C.; Rossel, C.; Rossell, M. D.; Erni, R.; Caimi, D.; Sousa, M.; Chelnokov, A.; Offrein, B. J.; Fompeyrine, J. A Strong Electro-optically Active Lead-free Ferroelectric Integrated on Silicon. *Nat. Commun.* **2013**, *4*, 1671.
(27) Van de Veire, T.; George, J.; Rijckaert, H.; Neyts, K.; Lauwaert, J.; Beunis, F.; Beeckman, J. In-plane Characterization of PZT Thin Films for the Creation of a General Impedance Model. *J. Appl. Phys.* **2021**, *129*, No. 094501.
(28) Tohge, N.; Takahashi, S.; Minami, T. Preparation of $PbZrO_3$-$PbTiO_3$ Ferroelectric Thin Films by the Sol-gel Process. *J. Am. Ceram. Soc.* **1991**, *74*, 67−71.
(29) Peng, Z.; Li, X.; Zhao, M.; Cai, H.; Xu, B. Fabrication of $Pb_{1-x}La_xTiO_3$ Ferroelectric Ceramic Nanocrystalline Thin Films. *Thin solid films* **1995**, *265*, 10−14.
(30) Ernstbrunner, E. Vibrational Spectra of Acetylacetone and its Anion. *Journal of the Chemical Society A: Inorganic, Physical* **1970**, 1558−1561.
(31) Mines, G.; Thompson, H. W. Infrared and Photoelectron Spectra, and Keto—enol Tautomerism of Acetylacetones and Acetoacetic Esters. *Proc. R. Soc. Lond. A* **1975**, *342*, 327−339.
(32) Almeida, L. A.; Habran, M.; dos Santos Carvalho, R.; Maia da Costa, M. E.; Cremona, M.; Silva, B. C.; Krambrock, K.; Ginoble Pandoli, O.; Morgado, E., Jr; Marinkovic, B. A. The Influence of Calcination Temperature on Photocatalytic Activity of TiO_2-Acetylacetone Charge Transfer Complex Towards Degradation of NO_x Under Visible Light. *Catalysts* **2020**, *10*, 1463.
(33) Zeitler, V. A.; Brown, C. A. The Infrared Spectra of Some Ti-O-Si, Ti-O-Ti and Si-O-Si Compounds. *J. Phys. Chem.* **1957**, *61*, 1174−1177.
(34) Moran, P. D.; Bowmaker, G. A.; Cooney, R. P.; Finnie, K. S.; Bartlett, J. R.; Woolfrey, J. L. Vibrational Spectra and Molecular Association of Titanium Tetraisopropoxide. *Inorganic chemistry* **1998**, *37*, 2741−2748.
(35) Bradley, D.; Holloway, C. Nuclear Magnetic Resonance and Infrared Spectral Studies on Labile Cis-dialkoxy-bis (Acetylacetonato) Titanium (IV) Compounds. *Journal of the Chemical Society A: Inorganic, Physical, Theoretical* **1969**, 282−285.
(36) Saxena, U.; Rai, A.; Mathur, V.; Mehrotra, R.; Radford, D. Reactions of Zirconium isopropoxide with β-diketones and β-keto-esters. *Journal of the Chemical Society A: Inorganic, Physical, Theoretical* **1970**, *0*, 904−907.
(37) Leaustic, A.; Babonneau, F.; Livage, J. Structural Investigation of the Hydrolysis-condensation Process of Titanium Alkoxides $Ti(OR)_4$ (OR= OPr^i, OEt) Modified by Acetylacetone. 1. Study of the Alkoxide Modification. *Chem. Mater.* **1989**, *1*, 240−247.
(38) Zhou, C.; Ouyang, J.; Yang, B. Retarded Hydrolysis-condensing Reactivity of Tetrabutyl Titanate by Acetylacetone and the Application in Dye-sensitized Solar Cells. *Mater. Res. Bull.* **2013**, *48*, 4351−4356.
(39) Morioka, H.; Yokoyama, S.; Oikawa, T.; Funakubo, H.; Saito, K. Spontaneous Polarization Change with Zr/(Zr+ Ti) Ratios in Perfectly Polar-axis-orientated Epitaxial tetragonal $Pb(Zr,Ti)O_3$ films. *Applied physics letters* **2004**, *85*, 3516−3518.
(40) Tita, S. P.; Magalhães, F. D.; Paiva, D.; Bertochi, M. A.; Teixeira, G. F.; Pires, A. L.; Pereira, A. M.; Tarpani, J. R. Flexible Composite Films Made of EMAA- Na+ Ionomer: Evaluation of the Influence of Piezoelectric Particles on the Thermal and Mechanical Properties. *Polymers* **2022**, *14*, 2755.
(41) Monga, S.; Sharma, N.; Mehan, N.; Mishra, Y. K.; Singh, A. Qualitative Analysis of PZT (52/48) MPB Using Different Synthesis Methods. *Ceram. Int.* **2022**, *48*, 31111−31120.
(42) Streiffer, S.; Parker, C.; Romanov, A.; Lefevre, M.; Zhao, L.; Speck, J.; Pompe, W.; Foster, C.; Bai, G. Domain Patterns in Epitaxial Rhombohedral Ferroelectric Films. I. Geometry and Experiments. *J. Appl. Phys.* **1998**, *83*, 2742−2753.
(43) Leclerc, G.; Poullain, G.; Bouregba, R.; Chateigner, D. Influence of the Substrate on Ferroelectric Properties of ⟨111⟩ Oriented Rhombohedral $Pb(Zr_{0.6}Ti_{0.4})O_3$ Thin Films. *Appl. Surf. Sci.* **2009**, *255*, 4293−4297.
(44) Fork, D.; Armani-Leplingard, F.; Kingston, J.; Anderson, G. Thin Film Epitaxial Oxide Optical Waveguides. *MRS Proc.* **1995**, *392*, 189.
(45) Park, C.-S.; Lee, J.-W.; Park, G.-T.; Kim, H.-E.; Choi, J.-J. Microstructural Evolution and Piezoelectric Properties of Thick $Pb(Zr,Ti)O_3$ Films Deposited by Multi-sputtering Method: Part I. Microstructural Evolution. *Journal of materials research* **2007**, *22*, 1367−1372.
(46) Ihlefeld, J. F.; Kotula, P. G.; Gauntt, B. D.; Gough, D. V.; Brennecka, G. L.; Lu, P.; Spoerke, E. D. Solution Chemistry, Substrate, and Processing Effects on Chemical Homogeneity in Lead Zirconate Titanate Thin Films. *J. Am. Ceram. Soc.* **2015**, *98*, 2028−2038.
(47) Silva, J.; Rodrigues, S.; Sekhar, K.; Pereira, M.; Gomes, M. Ferroelectric Properties of Pulsed Laser Deposited PZT (92/8) Thin Films. *Journal of Materials Science: Materials in Electronics* **2013**, *24*, 5097−5101.
(48) Yaseen, M.; Chen, X.; Ren, W.; Feng, Y.; Shi, P.; Wu, X.; Zhu, W. Effect of Annealing Temperature on Ferroelectric Electron Emission of Sol-gel PZT Films. *Ceram. Int.* **2013**, *39*, S471−S474.
(49) Khodaei, M.; Seol, D.; Seyyed Ebrahimi, S.; Park, Y. J.; Seo, H.; Kim, Y.; Baik, S. Ferroelectric and Piezoelectric Behavior of (111)-oriented $Pb(Zr_xTi_{1-x})O_3$ Thin Films on Cobalt Ferrite Nano-seed Layered Pt (111)/Si Substrate. *Journal of Materials Science: Materials in Electronics* **2014**, *25*, 1696−1702.
(50) Castellano, R.; Feinstein, L. Ion-beam Deposition of Thin Films of Ferroelectric Lead Zirconate Titanate (PZT). *Journal of applied physics* **1979**, *50*, 4406−4411.
(51) Pandey, S.; James, A.; Raman, R.; Chatterjee, S.; Goyal, A.; Prakash, C.; Goel, T. Structural, Ferroelectric and Optical Properties of PZT Thin Films. *Physica B: Condensed Matter* **2005**, *369*, 135−142.
(52) Lee, E. G.; Lee, J. K.; Kim, J.-Y.; Lee, J. G.; Jang, H. M.; Kim, S. J. Zr/Ti Ratio Dependence of the Deformation in the Hysteresis Loop of $Pb(Zr,Ti)O_3$ Thin Films. *Journal of materials science letters* **1999**, *18*, 2025−2028.
(53) Wang, Y.; Zhu, H.; Xue, Y.; Yan, P.; Ouyang, J. Microstructure Evolution with Rapid Thermal Annealing Time in (001)-Oriented Piezoelectric PZT Films Integrated on (111) Si. *Materials* **2023**, *16*, 2068.
(54) Feutmba, G. F.; Da Silva, L.; Singh, N.; Breyne, L.; De Geest, K.; George, J. P.; Bauwelinck, J.; Van Thourhout, D.; Yin, X.; Beeckman, J. High Frequency Characterization of PZT Thin-films Deposited by Chemical Solution Deposition on SOI for Integrated

High Speed Electro-optic Modulators. *Optical Materials Express* **2023**, *13*, 2120−2134.

https://doi.org/10.1021/acsami.4c07073
ACS Appl. Mater. Interfaces 2024, 16, 41134−41144